

# Instability Characteristics of Radar-Derived Mesoscale Organization Modes within Cool-Season Precipitation near Portland, Oregon\*

JEFFREY G. CUNNINGHAM

*U.S. Air Force Weather Agency, Norman, Oklahoma*

SANDRA E. YUTER

*Department of Marine, Earth and Atmospheric Sciences, North Carolina State University, Raleigh, North Carolina*

(Manuscript received 16 April 2013, in final form 18 January 2014)

## ABSTRACT

The instability characteristics associated with different radar-derived mesoscale organization modes are examined using six cool seasons of operational scanning radar data near Portland, Oregon, and operational sounding data from Salem, Oregon. Additionally, several years of Microwave Rain Radar Ka-band vertically pointing radar data from Portland and Merwin, Washington, are used to characterize the nature and occurrence of generating cells and fall streaks. The combination of a new metric, convective-stratiform intermittency, with the classification of radar reflectivity maps into convective and stratiform precipitation types was applied to periods when the freezing level was  $>1.4$ -km altitude. This method distinguishes periods with embedded convective within stratiform mesoscale organization from those that were mostly convective or mostly stratiform. Mesoscale organization occurs in a continuum of states with predominantly stratiform structure occurring most frequently. Generating cells in the snow layer are common in cool-season storms and are primarily associated with potential instability aloft. For mostly stratiform and embedded convective within stratiform 3-h periods, the vertically pointing radar data showed nearly ubiquitous fall streaks in the snow layer originating above 3-km altitude. Stronger generating cells enhanced reflectivity in the rain layer consistent with a seeder mechanism. Stronger generating cells were more common during embedded convection within stratiform than in mostly stratiform periods. Nearly all embedded periods have active or latent (potential) instability. Hydrostatic instability more typically occurred at higher altitudes for embedded convective within stratiform periods compared to mostly convective periods. The occurrence of vertical wind shear instability was primary below 2-km altitude and was not typically associated with levels with generating cells.

## 1. Introduction

Multiscale variations in precipitation are an important aspect of extratropical cyclones. Early studies examined the interrelationships among satellite-observed cloud, surface and upper-air synoptic patterns, and mesoscale precipitation (Nagle and Serebreny 1962; Elliott and

Hovind 1964; Kreitzberg and Brown 1970; Browning 1974; Hobbs and Locatelli 1978). These studies documented radar-observed bands ( $\sim 10^3$ – $10^4$  km<sup>2</sup>) of precipitation composed of smaller “cells” or “cores” ( $\sim 10$ – $10^2$  km<sup>2</sup>). Hobbs (1978) distilled information from previous work into a widely accepted schematic of five types of rainbands with the nomenclature based on the band’s position relative to the synoptic fronts: warm-frontal bands, warm-sector bands, cold-frontal bands, prefrontal cold-surge bands, and postfrontal bands.

Vertically pointing radar used by early investigators revealed that some rainbands contained “generating cells” in the ice layer that manifested as “mares’ tails” or fall streaks in the time–height plots of vertically pointing radar data (e.g., Marshall 1953; Fig. 2 in Hobbs 1978). In some cases, generating cells and their associated fall streaks in snow are sufficiently strong to enhance rainfall

---

\* Supplemental information related to this paper is available at the Journals Online website: <http://dx.doi.org/10.1175/MWR-D-13-00133.s1>.

---

*Corresponding author address:* Dr. Sandra E. Yuter, Department of Marine, Earth and Atmospheric Sciences, North Carolina State University, 2800 Faucette Dr., Jordan Hall Campus Box 8208, Raleigh, NC 27695-8208.  
E-mail: seyuter@ncsu.edu

in the rain layer. These stronger fall streaks appear as vertically continuous, localized enhancements in radar reflectivity that extend from the generating cells aloft all the way to the surface. Within a generating cell, snow grows preferentially larger and/or denser by a combination of riming and aggregation compared to nearby snow crystals formed outside a generating cell (Hobbs 1978). When this larger/denser ice particle melts, it produces a larger raindrop that in turn collects more mass as it falls through the rain layer as compared to the mass collected by smaller falling raindrops. Several authors (Matejka et al. 1980; Hobbs et al. 1980; Rutledge and Hobbs 1983) used the term “seeder feeder” to describe this process for rainbands within extratropical cyclones although the term is more usually defined as an orographic precipitation enhancement mechanism where the “feeder” cloud is a result of flow over topography (Browning and Hill 1981; Stoelinga et al. 2013). In this paper, we will use the more generic terms “generating cells” and “seeder cells” interchangeably to describe localized convective overturning in the snow layer that yields a fall streak. A generating cell observed in radar is defined as a small region of locally high reflectivity from which a trail of hydrometeors originates (Glickman 2000). Some sort of instability must be present for generating cells to form, but once formed they may be maintained by the release of latent heat.

Early work on mesoscale rainbands within extratropical cyclones inferred that generating cells within rainbands were produced by the lifting of shallow layers of potentially unstable air (e.g., Kreitzberg and Brown 1970; Hobbs and Locatelli 1978). Browning (1974) described potential instability within a “warm conveyor belt” that is released as the flow ascends over the warm front. Mesoscale precipitation areas in the warm sector and over the warm front appeared to be associated with elevated layers of potential instability, which produced convective seeder cells aloft (Browning et al. 1974). Parsons and Hobbs (1983) hypothesized that potential instability and conditional symmetric instability are the primary causal factors for warm-sector rainbands but dismissed internal gravity waves and vertical shear as likely candidates. Rosenow et al. (2014) used airborne cloud radar data to examine the structures of generating cells and elevated convection in the comma-head region of continental winter cyclones sampled during 2009–10 Profiling of Winter Storms (PLOWs; Rauber et al. 2014) field campaign. Dry air aloft intruded over the warm front in two of the three cases they examined and produced elevated convective cells with a 5-km horizontal scale. Additionally, deep stratiform clouds and cloud-top-generating cells ~1–2-km horizontal scale were observed in regions of the comma head without dry air intrusions.

Pacific Northwest (PNW) cool-season precipitation is predominantly stratiform (i.e., relatively steady and continuous). Embedded convective cells within stratiform precipitation often occur in the middle sector of storms (Nagle and Serebreny 1962), and locally increase total precipitation (Hobbs et al. 1980) and streamflow discharge (Westrick and Mass 2001).

Recent idealized cool-season orographic precipitation modeling studies exclude generating cells and seeder-related processes (both the elevated hydrostatic instability and microphysical response). In an idealized modeling study using only liquid microphysics (Kessler 1969), Fuhrer and Schar (2005) argued that a “marginally unstable” (potentially unstable) air mass transecting a mountain ridge leads to development of stratiform precipitation with embedded convection. They describe the development of embedded convection within a stratiform region as highly dependent on small-amplitude upstream perturbations that enhance the efficiency of the convective circulations. Using mixed-phase microphysics in a model-sensitivity study, Kirshbaum and Smith (2008) and Cannon et al. (2012) found that not all convection brings about more efficient conversion of condensation to precipitation. The profiles used in Fuhrer and Schar (2005), Kirshbaum and Smith (2008), and Cannon et al. (2012) were vertical profiles with only near-surface potential instability (decreasing equivalent potential temperature with increasing height). Cannon et al. (2012) recognized this limitation by stating “...some clouds that were unable to internally generate much precipitation in our simulations may become much more efficient when seeded from above.”

The conceptual model of Medina et al. (2007), based on data collected during the Oregon-centered Improvement of Microphysical Parameterization through Observational Verification Experiment (IMPROVE-1 and -2; Stoelinga et al. 2003), attributes elevated turbulence and generating cells to wind shear instability above blocked flow. In contrast, in their IMPROVE-1 case study from 1–2 February 2001, Evans et al. (2005) observed numerous generating cells in two elevated layers aloft as part of a forward-titled cold front (Schultz and Steenburgh 1999). Woods et al. (2005) observed potential instability associated with a forward-tilted cold front for the IMPROVE-2 13 December 2001 storm over the Oregon Cascades.

In this paper, we use multiyear operational radar data, upper-air soundings, and vertically pointing radar data to resolve the discrepancy between contrasting previous observational findings regarding the primary source of instability for generating cells in the PNW—potential instability aloft or wind shear instability. We also use the vertically pointing radar to examine the occurrence and

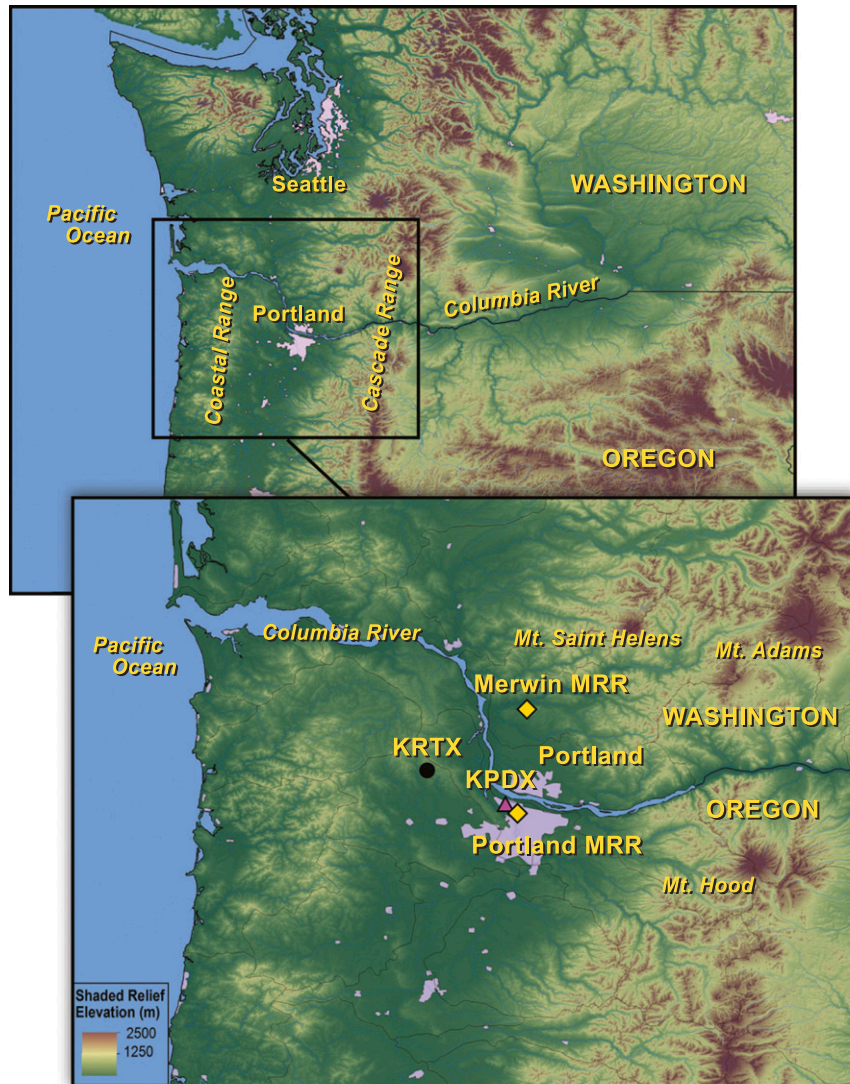


FIG. 1. Terrain maps of the study domain and location of instruments. (top) The major political and geographic features. (bottom) The Portland, OR, region with locations of important instruments indicated by various shapes. The black circle is the NWS WSR-88D operational scanning radar (KRTX), the pink triangle is the Portland International Airport NWS METAR (KPDX), the yellow diamond is the MRR vertically pointing radar, and the yellow star is the operational Salem, OR, sounding (KSLE). (Map courtesy of Nate Hardin.)

nature of generating cells within different mesoscale organization modes.

## 2. Data

Cool-season rainfall in the Pacific Northwest is a result of a combination of land-falling extratropical cyclones and orographic influences of the Coastal Mountains and the Cascade Range. Separating specific precipitation features and characteristics that are inherent in the cyclone from those that are a direct result of orographic

enhancement in observations is a challenge and can be ambiguous. This study focuses on radar and upper-air sounding data obtained over the Willamette Valley between the Coast Mountains and Cascade Range (Fig. 1) to deemphasize (but not eliminate) orographic factors. We build on data and methods from Yuter et al. (2011), which used a multiseason dataset obtained from 2003 to 2006 to study precipitation occurrence relative to terrain and several environmental factors.

The primary data for this study are observations from the Portland, Oregon (KRTX), National Weather Service

TABLE 1. Instruments used in this study.

Instrument name	Type of instrument	Variable used	Location	Period available	Time interval
KRTX WSR-88D	Scanning S-band precipitation radar	Reflectivity (dBZ)	45.71°N, 122.96°W	2002–08	6–10 min
KSLE NWS sounding	Upper-air balloon	Temperature, dewpoint temperature, wind speed, and direction	44.92°N, 123.02°W	2002–08	12 h (0000 and 1200 UTC)
KPDX NWS METAR	Surface meteorological observation	24-h precipitation total	45.59°N, 122.60°W	2002–08	Varies (at least 1 h)
MRR	Vertically pointing K-band radar	Reflectivity (dBZ), Doppler vertical velocity ( $\text{m s}^{-1}$ )	45.56°N, 122.53°W	2005–08 (Portland) and 2010–12 (Merwin)	1 min when available

(NWS) Weather Surveillance Radar-1988 Doppler (WSR-88D) obtained during the cool seasons (November–March) from 2002 to 2008. Upper-air soundings from the NWS upper-air rawinsonde located in Salem, Oregon (KSLE), were used for radar-identified storm periods from 2002 to 2008. Additionally, a METEK Inc. Microwave Rain Radar (MRR; Peters et al. 2002) provided vertically pointing radar data in Portland from 2005 to 2008 and in Merwin, Washington, from 2010 to 2012. Instrument locations are identified in Fig. 1, and details on the instruments are provided in Table 1. This study also used surface aviation routine weather report (METAR) observations at the Portland airport to identify rainy days and Geostationary Operational Environmental Satellite (GOES) infrared (IR) data to provide the large-scale cloudiness context.

#### a. Surface METAR at Portland International Airport (KPDX)

The KPDX METAR surface observation station is located at the Portland International Airport and is 32 km to the southeast of KRTX. KPDX provides standard hourly and special observations for the airfield. Daily precipitation data from KPDX were examined to identify days with 5 mm or more of precipitation following Yuter et al. (2011). To encompass the entire storm period, the day before and the day after each day with 5 mm or more rainfall were also examined to determine how much radar echo was present.

#### b. Portland, Oregon, WSR-88D (KRTX)

The KRTX WSR-88D is situated in the Willamette Valley (Fig. 1). During most instances when precipitation is observed in the domain, this radar is operated with a volume coverage pattern that yields a  $0.5^\circ$  elevation slice every 6 min. KRTX has an approximately  $0.93^\circ$  beamwidth [(Office of the Federal Coordinator for Meteorological Services and Supporting Research) OFCM 2006]. KRTX WSR-88D data are archived in level II format at the National Climatic Data Center

(NCDC) in Asheville, North Carolina, and are available online (NCDC 2012).

In contrast to Yuter et al. (2011), where the entire radar volume scan was interpolated into a three-dimensional volume, this study used only radar data from the  $0.5^\circ$  elevation angle of the volume scan to create a two-dimensional radar reflectivity map. We found that the identification of convective cells in this dataset (section 3a) performed best using a Cartesian interpolated single-elevation angle, which was seamless but had altitude increasing with range.

The level II polar data for the  $0.5^\circ$  elevation angle were interpolated to a  $2 \text{ km} \times 2 \text{ km}$  horizontal grid out to a 70-km range using the National Center for Atmospheric Research (NCAR) REORDER software (NCAR 2012). Two-dimensional interpolation of the single-elevation scan used Cressman weighting and an azimuthal radius of  $1.1^\circ$ . Selected storms were interpolated into three-dimensional Cartesian volumes with 2-km horizontal resolution and 1-km vertical resolution using Cressman weighting with an azimuthal radius =  $1.1^\circ$  and  $\Delta z$  radius = 1 km for the purpose of evaluating the convective-stratiform classification algorithm settings (section 3a).

We also used a more rigorous approach to removing data with ground-clutter contamination compared to Yuter et al. (2011). Data from the entire northwest quadrant of the radar are not used in the analysis because low hills consistently block the radar beam there. Additionally, a small set of local mountain peaks in other quadrants partially block the radar beam at a  $0.5^\circ$  elevation angle in standard atmospheric refraction conditions (Doviak and Zrnic 1993). Data were treated as ground clutter and removed from the analysis if an elevation grid point intersected a radar beam at a  $0.025^\circ$  elevation angle. This aggressive clutter removal accounts for partial beam blockage of the lowest  $0.5^\circ$  elevation angle scan. We use the term “radar domain” to refer to the  $10\,720 \text{ km}^2$  region of quality-controlled radar data used in the study.

We address potential brightband contamination (e.g., high radar reflectivity associated with partially melted

TABLE 2. Sample sizes of 3-h precipitation periods used in this study. Values in parenthesis indicate number of radar 3-h periods with soundings within  $\pm 1.5$  h.

	Cool season						Total 3-h periods
	2002–03	2003–04	2004–05	2005–06	2006–07	2007–08	
3-h periods							
No. with $>1000$ km <sup>2</sup> precipitation area	431	490	289	583	474	605	2872
No. with freezing level $<1.4$ km	153	238	150	330	217	425	1513
No. with freezing level $>1.4$ km	278	252	139	253	257	180	1359
Freezing level $>1.4$ km and							
No dominant mode	148	154	83	126	115	92	718 (167)
Dominant mode present	130	98	56	127	142	88	641 (171)
Dominant mode present and							
Mostly stratiform	93 (25)	65 (14)	38 (9)	79 (25)	75 (16)	36 (10)	386 (99)
Embedded convective within stratiform	23 (6)	14 (5)	7 (4)	22 (8)	35 (11)	25 (6)	126 (40)
Mostly convective	11 (1)	11 (4)	7 (3)	20 (4)	27 (8)	22 (7)	98 (27)
Other	3 (0)	8 (2)	4 (2)	6 (0)	5 (3)	5 (0)	31 (5)

particles at altitudes just below the  $0^{\circ}\text{C}$  level) in our analysis by applying minimum freezing level height and maximum range constraints to the radar dataset. We restrict analysis to the 3-h periods within 6 h of a sounding that exhibits a  $0^{\circ}\text{C}$  level  $>1.4$  km (1359 3-h periods over 281 calendar days, Table 2). At the 70-km maximum range, the  $0.5^{\circ}$  elevation scan is below 1.4-km altitude in standard refraction conditions. After applying the above quality control steps, significant precipitation 3-h periods were defined as having precipitation covering an area of  $\geq 1000$  km<sup>2</sup> and retained for further processing.

### c. Microwave rain radar

The NWS WSR-88Ds have insufficient vertical spatial resolution to routinely observe generating cells and fall streaks. We fill in this observation gap using an MRR, a vertically pointing Ka-band (24.1 GHz) radar (Löffler-Mang et al. 1999; Peters et al. 2002). The MRR provides information on the detailed structures of precipitation directly over the instrument, but this information is not representative of what is occurring in the entire scanning radar domain. The MRR has a beamwidth of  $1.5^{\circ}$ . For the Portland deployment, the MRR was set up with a vertical range up to 4.5-km altitude and a gate spacing of 150 m. For the Merwin deployment, the vertical range was up to 7.8-km altitude and the gate spacing was 250 m (Fig. 2). Radar reflectivity and Doppler vertical velocity  $V_D$  are recorded every 1 min. With the Ka-band radar, reflectivity values are subject to signal attenuation during heavy precipitation. The absolute magnitudes of reflectivity are unreliable above heavy precipitation regions. However, relative patterns of reflectivity are still useful for identifying fall streaks in snow. In the MRR data, “false fall streaks” can occur adjacent to columns of strongly attenuated reflectivity. In the Portland region, such strong attenuation in the snow layer is usually

a result of very high reflectivity ( $>40$  dBZ) in the rain layer.

The  $V_D$  for the MRR is defined in the vertical direction as  $V_D = V_F + V_A$ , where  $V_F$  is the hydrometeor fall velocity and  $V_A$  is the vertical motion of the air. The  $V_F$  is dependent on hydrometeor type. Positive values of  $V_D$  are moving toward the radar (i.e., down or toward the ground), and negative values are moving away from the radar. Doppler vertical velocity data are reliable through the entire column because they are not affected by signal attenuation.

### d. Upper-air sounding at Salem, Oregon (KSLE)

The Salem NWS upper-air sounding (KSLE) is the nearest operational sounding available for the study domain (89 km south of KRTX) and is available every 12 h. KSLE data are available for the entire 6-yr study period. We use soundings to characterize the environment associated with different mesoscale organization modes derived from the radar data (section 3). In the Pacific Northwest, conditions are usually saturated or nearly saturated near the surface during extratropical cyclone passage.

Compositing or averaging soundings, as done in Ralph et al. (2005), can potentially mask important hydrostatic instabilities aloft when the exact altitude of the unstable layer varies across storms. We examine the frequency of occurrence with altitude of various types of instabilities rather than averaging to minimize this potential masking. Sounding data were interpolated to 10 m and instability metrics were calculated for 500-m layers. We computed the most unstable parcel convective available potential energy (MUCAPE) as defined by Doswell and Rasmussen (1994). The advantage of this method is that it determines the CAPE of the most unstable parcel within the lowest 300 mb (approximately 3 km), which may or may not be the surface parcel.

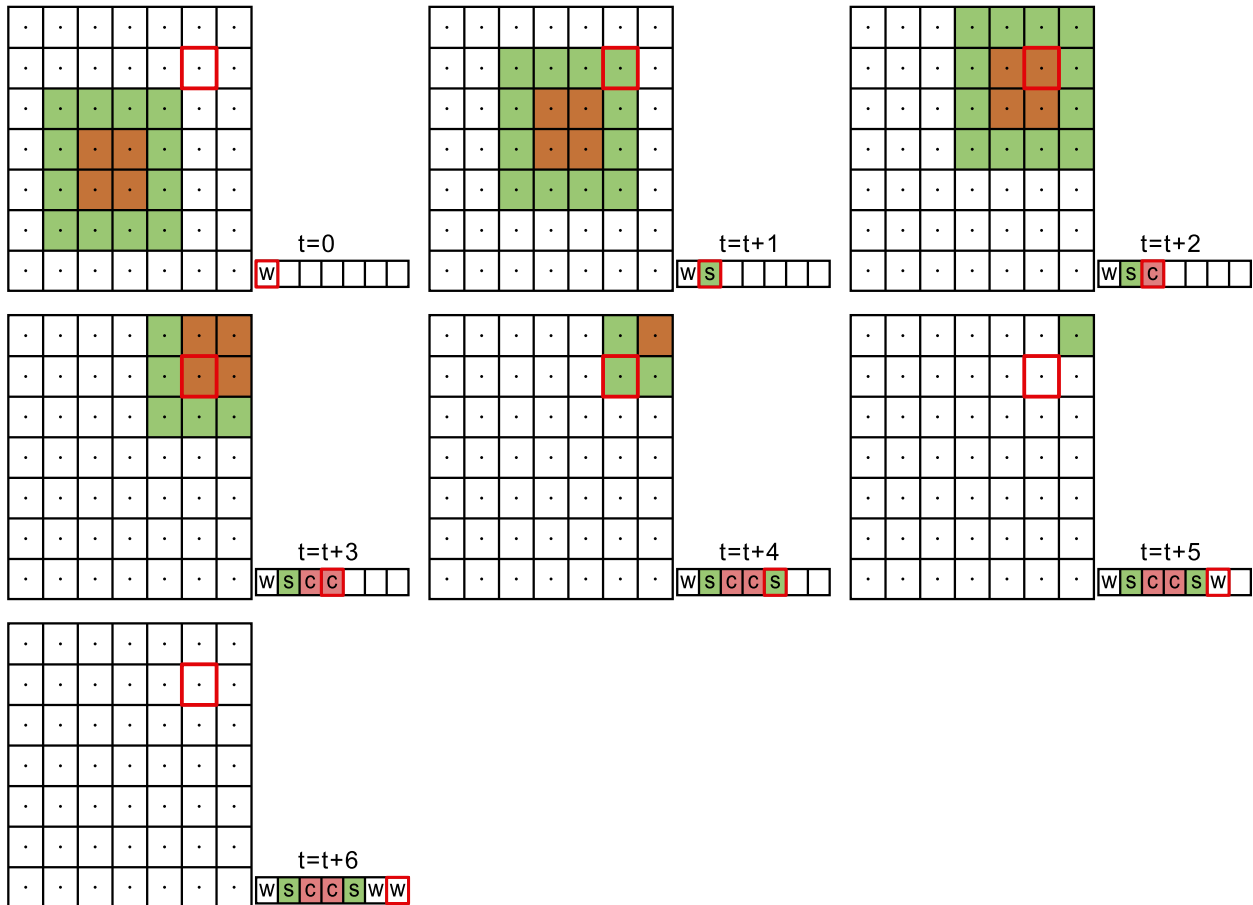


FIG. 2. Illustration of a simplified time-ordered sequence of precipitation type used to determine convective-stratiform intermittency. Each panel shows a CONVSF map and is labeled with a corresponding time  $t = 0$  to  $t = t + 6$ . In this example, a hypothetical convective cell moves from the bottom left to the upper right. As the cell moves over the red highlighted box, the precipitation type within the red box is added to the time-ordered sequence of precipitation types at that grid point (bottom right of each panel). Convective precipitation is indicated by the color red, stratiform precipitation by green, and white indicates a grid point identified as either weak echo or no echo.

We calculated the change in equivalent potential temperature with height  $d\bar{\theta}_e/dz$  for each 500-m layer in the soundings and determined which layers had  $d\bar{\theta}_e/dz < 0$ . If a layer of atmosphere is saturated and  $d\bar{\theta}_e/dz < 0$ , the layer of air is considered moist absolutely unstable. If the layer of air is unsaturated and  $d\bar{\theta}_e/dz < 0$ , the layer is considered potentially unstable. A layer of air that is potentially unstable can become moist absolutely unstable when saturation occurs through layer lifting or evaporation of water into the layer. The presence of either  $\text{MUCAPE} > 0 \text{ J kg}^{-1}$  or potential instability is evidence of hydrostatic instability within the column (Markowski and Richardson 2010).

A moist Richardson number (Ri), based on a simplified version of the moist Brunt–Väisälä frequency  $N_m$ , is used to calculate vertical wind shear instability (Kelvin–Helmholtz instability), where  $\text{Ri} = N_m^2 / (\partial \bar{u} / \partial z)^2$  and  $N_m = [(g/\theta_e)(\Gamma_m/\Gamma_d)(\partial \bar{\theta}_e / \partial z)]^{1/2}$  [adapted from Markowski

and Richardson (2010)]. Kelvin–Helmholtz stability is guaranteed for  $\text{Ri} > 0.25$ ; however,  $0 < \text{Ri} < 0.25$  is required, but not sufficient, for instability.

Logically, cases should be examined for hydrostatic instability first, before conditional symmetric instability (Schultz and Schumacher 1999; McCann 1995). Assessment of conditional symmetric instability requires thermodynamic data with high three-dimensional resolution, and such data were not available for this study.

### 3. Methods

We introduce a method that utilizes the time-ordered sequence of precipitation type classified at each individual grid point over 3-h periods. The new metric is used to examine the joint temporal and spatial variability at  $4\text{-km}^2$  grid points within the radar domain. While periods that are primarily convective or stratiform can be

distinguished using spatial metrics alone, information on the time-ordered sequence is needed to identify the intermittency characteristic of embedded convection within stratiform. The new method permits us to automatically discriminate between mesoscale regions with embedded convection within stratiform—characterized by many grid points within the domain with short intervals of convective precipitation alternating with stratiform precipitation—from mesoscale regions transitioning between more steady convective and stratiform precipitation (or vice versa).

#### *a. Convective-stratiform (CONVSF) algorithm*

We first identify the precipitation spatial structure at each 4-km<sup>2</sup> grid point in the two-dimensional interpolated radar reflectivity from the 0.5° elevation angle scan using the CONVSF algorithm. This algorithm was originally defined by Churchill and Houze (1984). It was later adapted and generalized by Steiner et al. (1995), Houze (1997), and Yuter et al. (2005) for different grid point spatial scales and radar characteristics. Churchill and Houze (1984) developed the algorithm for radar data from the tropics in an effort to objectively quantify the unique contributions of stratiform and convective precipitation to rainfall totals. The algorithm is a practical application of the conceptual framework described in Houze (1997) for identifying convective radar echoes with two-dimensional radar data. The algorithm categorizes every pixel in a two-dimensional gridded data field as convective, stratiform, or weak echo, beginning with convective pixels first. Beam filling reduces the observed magnitudes of reflectivity for precipitation structures that are smaller than the radar resolution volume and/or interpolated grid spacing (Rinehart 2004). The CONVSF algorithm settings need to be tuned for a particular radar (factoring in beamwidth, calibration, scan strategy, sensitivity, and potential attenuation issues) and grid spacing [for details see appendix B in Yuter et al. (2005) and Fig. 8 in Steiner et al. (1995)]. The tuning calibrates the specific coefficient value against the vertical cross sections of radar echoes in regions sufficiently close to the radar where it is possible to clearly distinguish between vertically oriented convective cells and a horizontal radar bright band.

The CONVSF algorithm was designed to work in the tropics, so some adjustments to the criteria were required for it to work with data collected by the NWS KRTX radar. Compared to deep tropical convection, radar reflectivities within precipitation cores in the Pacific Northwest are typically less intense and the relative difference between the reflectivity value in a precipitation core and the surrounding echo is smaller. For the identification of convective cores, we turned off the

intensity requirement and use only the detection of peakedness (sharp gradients) within the reflectivity field following Yuter and Houze (1997). We also increased the algorithm's sensitivity to horizontal reflectivity gradient changes by adjusting parameter  $a$  in Eq. (B1) of Yuter and Houze (1997) from a setting of 8 to a setting of 4. The setting was chosen by examining several dozen cases using a range of parameter  $a$  values and by evaluating the resulting classifications with vertical cross sections derived from three-dimensional interpolated radar volumes (section 2b). Following James and Houze (2005) and Yuter et al. (2011), echoes with radar reflectivity less than 13 dBZ (equivalent rain rate of approximately 0.2 mm h<sup>-1</sup>) were classified as weak echoes. For purposes of the classification of precipitation structures, we do not distinguish between weak echo and no detectable echo.

To function properly, the CONVSF algorithm requires that input radar reflectivity field be entirely within the rain layer. This requirement limits the application of the algorithm for this study to periods when the freezing level is >1.4-km altitude (see section 2b).

#### *b. Measures computed over 3-h periods*

We use the set of ~30 CONVSF maps for each 3-h period to determine the time-ordered sequence of precipitation type for each grid point. Use of 3-h periods is a compromise to ensure a sufficiently large number of radar volumes to perform calculations (approximately 30 volumes during a 3-h period) while also minimizing significant evolution and advection of storm structures.

To illustrate application of the method, Fig. 2 shows a series of seven simplified CONVSF maps with a convective cell moving from the bottom left to the upper right. The time sequence of precipitation structure within the red highlighted grid point is progressively shown at the bottom right of each subplot. As the cell moves over the highlighted box, the precipitation type changes from weak echo ( $t = 0$ ) to stratiform ( $t + 1$ ) to convective ( $t + 2$  and  $t + 3$ ) to stratiform ( $t + 4$ ) to weak echo ( $t + 5$  and  $t + 6$ ). Storing the time-ordered sequence of precipitation type for each grid point permits calculation of maps of several variables related to precipitation occurrence and intermittency as described below.

### 1) FREQUENCY OF PRECIPITATION

Frequency of precipitation is a common calculation used to identify geographic locations of preferred or enhanced precipitation (James and Houze 2005; Ellis et al. 2009; Panziera and Germann 2010; Yuter et al. 2011; Biasutti et al. 2012):

$$\begin{aligned} &\text{frequency of precipitation} \\ &= 100\% \times \frac{\text{number of precipitating pixels}}{\text{number of opportunities}}. \end{aligned}$$

A precipitating pixel is defined as any grid point categorized as either convective or stratiform. The total number of opportunities for the time period is the total number of radar volumes in 3 h. A frequency of precipitation equal to 100% means that precipitation  $\geq 13$  dBZ is always occurring at a grid point, whereas a frequency of precipitation equal to zero means that precipitation  $\geq 13$  dBZ never occurs at a grid point.

The frequency of precipitation maps are used to determine the subset of grid points where precipitation occurs at least 30% of the time during the 3-h period. Application of this threshold focuses analysis on the portions of the radar domain with one or more hours of rainfall over the 3-h period. These precipitating grid points are in turn used to calculate the frequency of convective precipitation and the convective-stratiform intermittency as defined in the following sections.

2) FREQUENCY OF CONVECTIVE PRECIPITATION

The frequency of convective precipitation is defined as

$$\begin{aligned} &\text{frequency of convective precipitation} \\ &= 100\% \times \frac{\text{number of convective pixels}}{\text{number of precipitating pixels}}. \end{aligned}$$

Frequency of convective precipitation equal to 100% means that the precipitating grid point is always identified as having a convective precipitation structure while a frequency equal to zero means that a precipitating grid point always has a stratiform precipitation structure. A frequency of convective precipitation equal to 50% means that the precipitating grid point is stratiform precipitation half of the time and convective precipitation the other half of the time.

3) CONVECTIVE-STRATIFORM INTERMITTENCY

A new measure, convective-stratiform intermittency, uses the time-ordered sequence of precipitation types to determine the relative amount of time the precipitation remains as either convective or stratiform before changing to the other. Convective-stratiform intermittency is defined as

$$\begin{aligned} &\text{convective-stratiform intermittency} \\ &= 100\% \times \frac{\text{number of transitions}}{\text{number of precipitation opportunities}}. \end{aligned}$$

Low values of convective-stratiform intermittency imply the 3-h period experiences longer periods of either

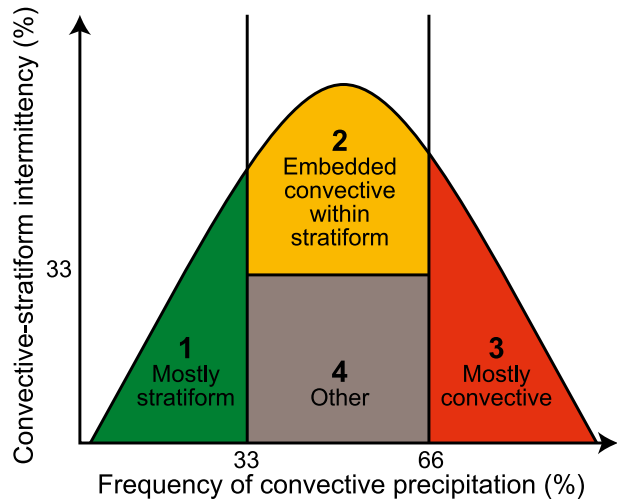


FIG. 3. The mapping of convective-stratiform intermittency and frequency of convective precipitation values to categorical descriptions used for determination of mesoscale organization mode.

convective or stratiform precipitation before changing. High values indicate relative short periods of either convective or stratiform precipitation before transitioning to the other type.

4) MESOSCALE ORGANIZATION MODES WITHIN THE RADAR DOMAIN

We seek to identify 3-h periods that are reasonably representative samples of distinct spatial-temporal mesoscale organization modes. To do this, we construct the joint frequency distribution of convective frequency and convective-stratiform intermittency for each 3-h period and use a combination of precipitation area and the relative number of grid points in each portion of the joint frequency phase space to determine if a dominant mesoscale organization mode is present.

We assigned descriptive labels to regions within the joint frequency distribution phase space (Fig. 3). The mostly stratiform mesoscale organization category has a frequency of convective precipitation less than 33%. The embedded convective within stratiform has a frequency of convective precipitation less than 66% but more than 33% and convective-stratiform intermittency greater than 33%. Mostly convective mesoscale organization is defined as frequency of convective precipitation greater than 66%. The “other” mode is defined as convective or stratiform for approximately half of the time with a low convective-stratiform intermittency (<33%). Although the boundaries are helpful for description and interpretation, it is also important to remember that the convective-stratiform intermittency and frequency of convective precipitation phase space is actually a continuum.

To determine if a dominant mode is present, we first find which region in the joint frequency distribution has the most number of grid points using the region boundaries in Fig. 3. If that number of grid points represents more than a quarter of the area with precipitation (at any frequency) in the 3-h period then a dominant mode is present. Three-hour periods not meeting these criteria are labeled as having “no dominant mode.” Details on how these criteria affect sample sizes are provided in section 4a.

For illustration purposes, each row in Fig. 4 contains a radar reflectivity map (left column) and the corresponding CONVSF map (middle column) for an individual radar scan within selected 3-h period. Information from across the 3-h period is combined in the right column of Fig. 4, which shows the joint frequency distributions of the 4-km<sup>2</sup>, 3-h gridpoint values.

In the first row, the joint distribution of convective frequency and convective-stratiform intermittency has a statistical mode (highest values in the scatter density plot) corresponding to a low frequency of convective (i.e., overwhelmingly stratiform) and a low intermittency (few transitions between convective and stratiform). These joint characteristics of the distribution mode are labeled as “mostly stratiform” mesoscale organization. In the second row in Fig. 4, the joint distribution plot has a statistical mode centered near the 40% values of both convective frequency and intermittency. These moderate values are consistent with a precipitation structure that was roughly equal portions convective and stratiform that also transitioned frequently between convective and stratiform precipitation types as it passed over grid points. Examination of time sequences of radar data confirm that this statistical mode corresponds to “embedded convective within stratiform” mesoscale organization. The third row in Fig. 4 shows an example 3-h period that has high convective frequency (~70% of time convective) and few transitions. We label 3-h periods with joint distributions similar to this as “mostly convective” mesoscale organization. The fourth row in Fig. 4 has a statistical mode with a convective frequency value near 50% and intermittency value of about 20%, lower than that in the example in the second row. The 3-h periods with these joint frequency distribution characteristics had relatively steady convective precipitation that changed to relatively steady stratiform (or vice versa). These periods occurred rarely (31 out of 1359 3-h periods) and are labeled other. Last, row 5 in Fig. 4 illustrates a joint frequency distribution with no dominant mode. In these cases, there is often a small number of precipitating pixels (as illustrated in this example) and/or a mixture of mesoscale structures.

### c. Evaluation of mesoscale organization mode classification relative to IR cloud structures

On a storm-to-storm basis, the quality of available model reanalysis fields varied so we use satellite data to evaluate the mesoscale organization mode classification. GOES IR images of the Pacific Northwest region for all significant precipitation days over 4 cold seasons (2002–03, 2003–04, 2004–05, and 2005–06) were manually examined to determine the location of the study domain relative to the extratropical cyclone’s cirrus cloud shield (i.e., high cloud shield) following an approach similar to Bader et al. (1995). The methods described in Bader et al. (1995, their chapters 3 and 4) provide guidelines for the interpretation of satellite imagery relative to the conceptual models of Browning (1986). The location of the 240 km × 240 km study domain was categorized as covered by 1) low/middle clouds east (ahead of) the cirrus cloud shield (no upper-level cloud in the domain), 2) central cirrus cloud shield, 3) western portion of the cirrus cloud shield near the cold front (within ~100 km of the western edge of the cirrus cloud shield), 4) low/middle cloud west (behind) the cirrus cloud shield (cold sector, primarily low-level cellular clouds, free of upper-level clouds), or 5) other. The other category included cloud locations near the inferred low pressure center. Given the limitations of the GOES IR data, no attempt was made to distinguish cold-frontal type, so the cold front could be oriented with a “traditional” tipped-back cold front or with a forward-tilted cold front. Also, no attempt was made to precisely locate the warm front.

Overall, the occurrence of different mesoscale organization modes relative to extratropical cyclone cloud structures (Table 3) were found to be consistent with the conceptual models from Nagle and Serebreny (1962), Hobbs (1978), and Browning and Monk (1982). Mostly stratiform precipitation occurred most frequently (>50%) beneath the central cirrus cloud shield. Embedded convective within stratiform precipitation occurred most frequently (~40%) in the western portion of the cirrus cloud shield near the cold front. Mostly convective precipitation occurred most frequently (>50%) within the cold sector associated with low and middle cloud west of the cirrus cloud shield. The other category of mesoscale organization occurred in a variety of cloud settings consistent with this radar-derived category representing transitional states among the categories.

### d. Statistical significance testing

Two-sample permutation tests were performed [section 5.3.3 of Wilks (2006)] to determine if the distributions of measurements at each level within vertical profiles represented distinct populations. The goal was

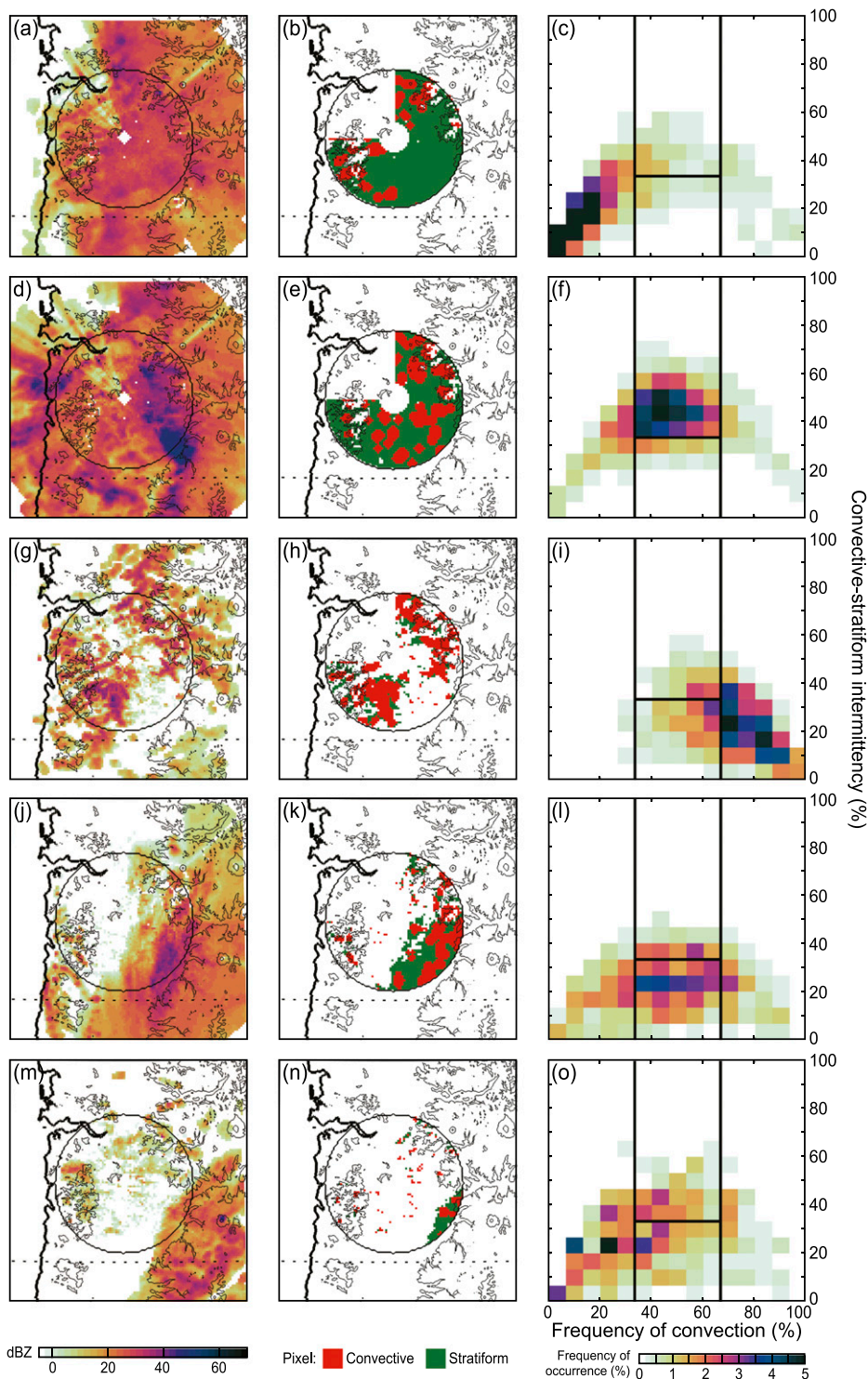


FIG. 4. Examples of different temporal-spatial mesoscale organization modes. Different times are shown in each row. (a),(d),(g),(j),(m) A map of KRTX radar reflectivity based on the 0.5° elevation angle scan and (b),(e),(h),(k),(n) the corresponding CONVSF map. Pixels are designated convective (red), stratiform (green), and weak echo or no echo (white). (c),(f),(i),(l),(o) The joint frequency distribution of frequency of convective precipitation and convective-stratiform intermittency for the associated 3-h periods. (a)–(c) Corresponds to a mostly stratiform period centered at 1200 UTC 27 Dec 2005. (d)–(f) Corresponds to an embedded convective within stratiform period centered at 0600 UTC 31 Dec 2005. (g)–(i) Corresponds to a mostly convective period centered at 0300 UTC 1 Jan 2006. (j)–(l) Corresponds to an “other” period centered at 2100 UTC 31 Dec 2005. (m)–(o) Corresponds to a no dominant mode period centered at 0000 UTC 8 Nov 2006.

TABLE 3. Evaluation of radar-derived mesoscale organization modes relative to IR cloud characteristics.

IR cloud description	Mostly convective	Embedded convective within stratiform	Mostly stratiform	Other
Low/middle cloud east of cirrus cloud shield	16%	20%	23%	16%
Central cirrus cloud shield	6%	23%	57%	16%
Western portion of cirrus cloud shield near cold front	14%	39%	16%	16%
Low/middle cloud west of cirrus cloud shield (cold sector)	53%	6%	1%	11%
Other clouds (includes near low pressure center)	10%	12%	4%	36%
Total No. of 3-h samples examined for each mesoscale organization mode	50	69	276	22

to assess to what degree profile characteristics from mostly stratiform, embedded, and mostly convective 3-h periods were significantly different. The null hypothesis was that the two empirical samples were drawn from the same sample distributions. For example, the observed distributions of wind speed at 2-km altitude from  $A$  = embedded convective within stratiform and  $B$  = mostly stratiform 3-h periods. The test statistic employed is the difference in percentile values of the two sample distributions being compared (e.g., numerical difference in values between the 25th percentile of distribution  $A$  and the 25th percentile of distribution  $B$ ). In our significance testing, we compute the test statistic for the 25th, 50th, and 75th percentiles. For each percentile, the original test statistic is calculated using the empirical distributions  $A$  and  $B$ . The two empirical distributions  $A$  and  $B$  are then pooled together. A null distribution of the test statistic is generated by calculating the test statistic on two pseudodistributions (equal in size to the original two empirical distributions)  $n$  times. The two pseudodistributions are generated by randomly drawing from the pooled distribution over a large number of trials (e.g., 10 000). The  $p$  value for this test is calculated by dividing the number of times the null distribution of the test statistic is larger than the original test statistic by total number of trials. With this  $p$  value, the hypothesis can be rejected or not rejected depending on the confidence level required (alpha level). For this research, an alpha level of 95% was required for rejecting the null hypothesis. A rejection of the null hypothesis means the odds of getting a difference as large as what was observed through random sampling are acceptably small. If the null hypothesis is rejected for the statistical tests at all three of the 25th, 50th, and 75th percentiles, we describe the distributions as significantly different.

## 4. Results

### a. Observational filter

As discussed in section 3a, in this study the application of the CONVSF algorithm is limited to periods with 0°C levels >1.4-km altitude. Hence, entire storms and

portions of storms when the freezing level is lower than 1.4-km altitude are not included in the analysis of mesoscale organization. Our results are valid only for the storms and portions of storms with deeper rain layers. Based on the conceptual models of Nagle and Serebreny (1962), Hobbs (1978), Medina et al. (2007), and others, we expect that periods within extratropical cyclones with shallower rain layers will have different proportions of mesoscale precipitation structures and stability characteristics than periods with deeper rain layers (higher freezing levels). Other environmental conditions being equal, deeper rain layers are associated with larger water vapor fluxes (Zhu and Newell 1998; Bao et al. 2006; Lin et al. 2013). Deeper rain layers, rainfall intensity, and long duration of rainfall are three factors that contribute to increased landslide potential (Baum and Godt 2010) and river flooding in this region (Yuter et al. 2011).

Figure 5 shows the six cool-season time series of storms examined in this study and distinguishes between periods with freezing levels above and below 1.4-km altitude. Depending on the individual storm, the periods with higher freezing levels can intersperse, toward the beginning, or toward the end of individual storms (Fig. 5). The number of storms varies month by month. A total of 29 of the 30 months of radar data analyzed had at least one storm meeting the minimum area and >1.4-km altitude freezing level criteria (Fig. 5).

The criteria used for determining if a dominant mode was present [section 3b(4)] indirectly favored larger precipitation areas. In total, 99% of periods with precipitating pixels (precipitation frequency >30%) covering at least 8000 km<sup>2</sup> (equivalent to ~90 km × ~90 km) of the radar domain had a dominant mode. The total number of and relative fraction of 3-h periods with freezing levels >1.4-km altitude and classified into a particular mesoscale organization mode varies season to season (Table 2). The largest sample (278 3-h periods) and largest proportion of (65%) of 3-h periods with freezing levels >1.4-km altitude occurred over the 2002–03 cool season. The smallest sample (139 3-h periods) occurred in the 2003–04 cool season and the smallest relative proportion (30%) occurred in the 2007–08 cool

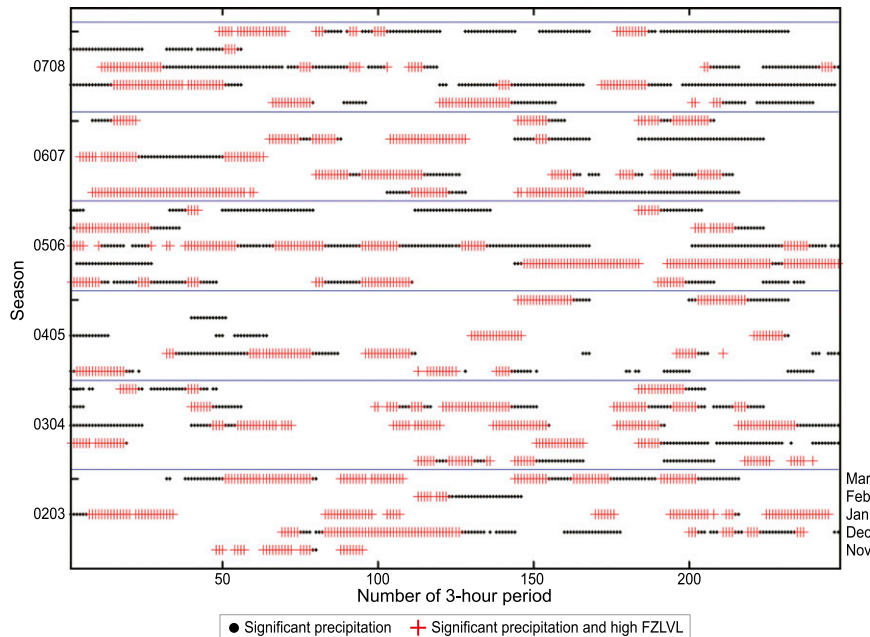


FIG. 5. (from bottom to top) Time series of storms examined in the 2002–03 through 2007–08 cool seasons. Each row represents a month. The 3-h periods with precipitation area  $>1000 \text{ km}^2$  within the radar domain are shown as circles for times when the freezing levels were  $<1.4\text{-km}$  altitude and as crosses for freezing levels  $>1.4\text{-km}$  altitude.

season. In comparison, Medina et al. (2007) examined eight storm events over the equivalent of 88 3-h periods from the IMPROVE-2 field project (Stoelinga et al. 2003). It is likely that not all the 88 3-h periods from Medina et al. (2007) met the precipitation area and frequency requirements used in this study.

Figure 6 shows the joint probability distribution of convective precipitation frequency and convective-stratiform intermittency for all radar grid points analyzed during the 1359 3-h periods with  $0^\circ\text{C}$  level  $>1.4\text{-km}$  altitude. This plot illustrates the continuum of observed states and the relative prevalence of mostly stratiform, embedded, and mostly convective characteristics of the  $4 \text{ km}^2$  3-h gridpoint samples. In any given 3-h period, individual grid points in the radar domain are most likely to be covered by stratiform precipitation. The outer boundaries of the observed phase space of convective precipitation frequency and convective-stratiform intermittency may be useful as numerical model evaluation metrics. For model output at sufficient temporal resolution ( $\sim 6$  min), the methods described in section 3 can be applied to model-derived reflectivity fields to yield analogous plots.

#### b. Wind and humidity profiles associated with different mesoscale organization modes

Of the 641 3-h periods with a dominant mesoscale organization mode within the radar domain, 60% were

categorized as mostly stratiform, 20% as embedded convective within stratiform precipitation, and 15% as mostly convective precipitation (Table 2). To document the thermodynamic characteristics associated with each mesoscale organization mode, we need to examine 3-h periods when a distinct organization mode is present and

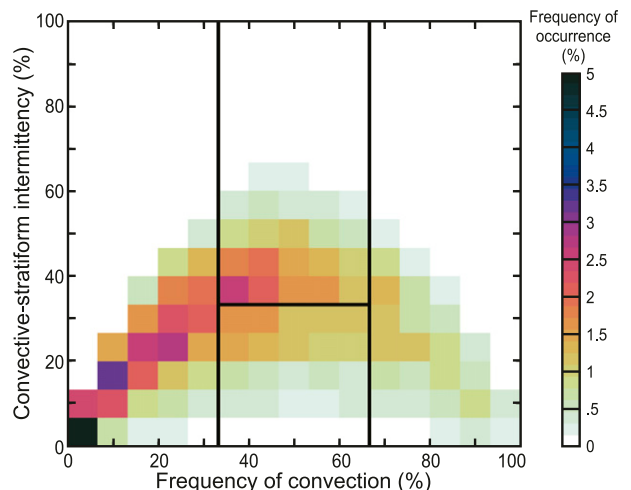


FIG. 6. Joint probability distribution of convective frequency and convective-stratiform intermittency for  $4 \text{ km}^2$  gridpoint data during the 1315 3-h periods when freezing levels were  $>1.4 \text{ km}$  (over 1.6 million gridpoint samples). The frequency of occurrence for each bin is indicated by the shading.

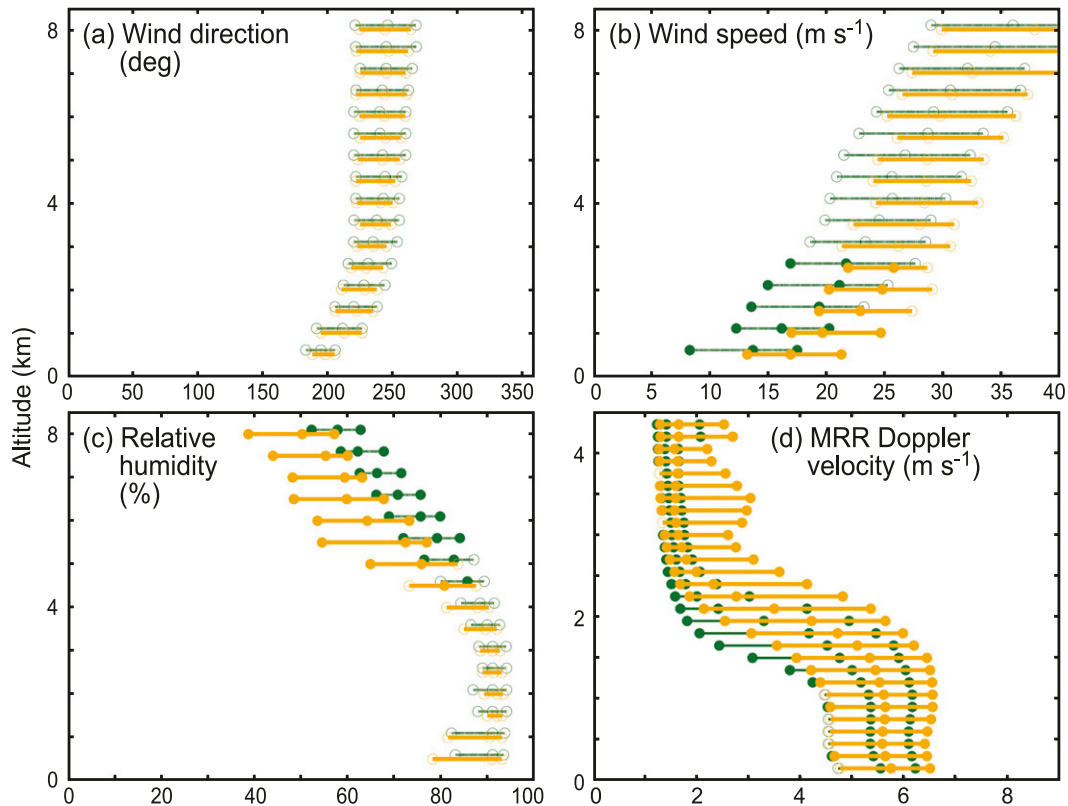


FIG. 7. Comparisons of profiles of sounding variables and MRR Doppler velocity between embedded convective within stratiform (gold) and mostly stratiform precipitation (green) mesoscale organization modes. (a) Wind direction ( $^{\circ}$ ), (b) wind speed ( $\text{m s}^{-1}$ ), (c) relative humidity (%), and (d) MRR Doppler velocity ( $\text{m s}^{-1}$ ). Note the different scale for altitude in (d) compared to the other panels. Circles are the 25th, 50th, and 75th percentiles. Filled circles represent percentile differences that are statistically significant (alpha level 95%). Unfilled circles represent percentile differences that are not statistically significant.

when a sounding is launched. These requirements constrain our sample size for the sounding analysis to 166 3-h periods (Table 2, we exclude the other category since there are only five soundings in this category). Oversampling of one storm is unlikely since there is a 12-h minimum time between consecutive analyzed 3-h radar-sounding pairs. A complete listing of soundings used in this analysis is provided in the online supplement.

Both the mostly stratiform and embedded mesoscale organization modes had similar wind profiles. Winds were from  $180^{\circ}$  to  $225^{\circ}$  at 1-km altitude (Fig. 7a) veering to  $200^{\circ}$  to  $250^{\circ}$  by 4-km altitude. The mostly convective mesoscale organization mode (not shown) was typically accompanied by more westerly wind (from  $200^{\circ}$  to  $250^{\circ}$  at 1 km and  $225^{\circ}$  to  $275^{\circ}$  at 4-km altitude) throughout the column.

There was a statistically ( $p \leq 0.05$ ) and meteorologically significant difference between wind speeds for stratiform and embedded mesoscale organization modes. Embedded 3-h periods had wind speeds  $3\text{--}5 \text{ m s}^{-1}$  higher than mostly stratiform 3-h periods (Fig. 7b) from near

the surface to 8-km altitude. Calculations of vertical wind shear do not show a statistically significant difference between the mostly stratiform and embedded modes. It is unclear whether the increase in total wind speed is due to increased convective activity or if the increased wind speed is related to a change in the mesoscale or synoptic environment leading to increased convective activity. The higher wind speeds could simply be due to a tighter pressure gradient near the surface or upper cold front. Higher wind speeds could also increase the amount of orographic lifting over the coastal mountains (i.e., higher cross-barrier winds could lift potentially unstable layers, causing destabilization).

Moisture profiles for mostly stratiform and embedded precipitation indicated near-saturated conditions from the surface to 3 km (relative humidity from 80% to over 90%; Fig. 7c). Above 3 km, the relative humidity decreased more rapidly for embedded compared to mostly stratiform precipitation. Mostly convective 3-h periods were nearly saturated from surface to approximately 2 km (not shown). Between 2- and 5-km altitude, relative

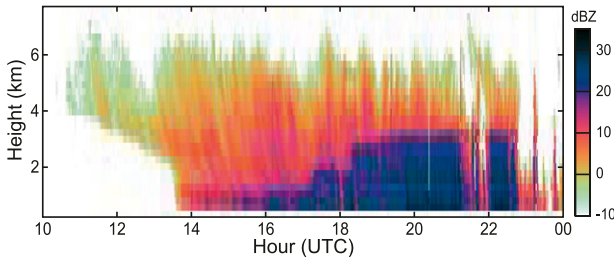


FIG. 8. An example of fall streaks in a time–height plot of MRR radar reflectivity data from Merwin, WA, from 1100 to 2300 UTC 11 Dec 2010. Some fall streaks have a clear extension from the snow layer into the rain layer.

humidity in the mostly convective mode decreased rapidly to values between 20% and 50% (not shown).

### c. MRR observed fall streaks and Doppler velocities

Consistent with vertically pointing radar datasets obtained in the 1970s during the University of Washington’s Cyclonic Extratropical Storms project (CYCLES; e.g., Hobbs and Locatelli 1978), visual examination of MRR vertically pointing radar reflectivity data from Portland for three cool seasons and from Merwin for two cool seasons found nearly ubiquitous fall streaks within the snow layer. Fall streaks are readily identified in time–height plots by local maxima in reflectivity that exhibit continuity in time with decreasing height (e.g., Fig. 8). Based on the three cool seasons of MRR data from Portland, snowfall streaks were visually identified in nearly 90% of mostly stratiform 3-h periods, 95% of embedded 3-h periods, and nearly 70% of mostly convective 3-h periods. Stronger fall streaks within snow could also be seen to enhance reflectivity in the rain layer consistent with a seeder mechanism (larger/denser snow melts into larger raindrops that collect more mass than smaller raindrops). The height of the earliest detectable snow fall streak varied, but most snow streaks began above 3 km. Generating cells are inferred to occur near the top of the fall streaks within the snow layer. Snow region fall streaks were of lower magnitude reflectivity and were more diffuse (e.g., low contrast) for a larger proportion (40%) of mostly stratiform periods compared to the embedded periods (only 10% of periods were diffuse). These more diffuse fall streaks had a smaller impact on the rain layer reflectivity and surface precipitation variability.

MRR Doppler vertical velocities had higher magnitudes and larger variability for embedded periods compared to mostly stratiform periods, particularly within the snow layer and to some extent in the rain layer, over the three seasons when the MRR was in Portland (Fig. 7d). Higher MRR Doppler vertical velocity values imply higher hydrometeor fall velocity (larger particles) and/or

higher downdraft velocity. The percentile differences between the distributions of Doppler vertical velocity for embedded 3-h periods and mostly stratiform 3-h periods were statistically significant for most vertical levels. Higher values of and larger variability in Doppler vertical velocity are consistent with stronger generating cells yielding large particles. Interpretation of reflectivity distributions is more complex due to possible signal attenuation; therefore, the MRR reflectivity data are not presented as vertical profile distributions.

### d. Instability characteristics

The 166 KSLE soundings corresponding to 3-h periods with a dominant mesoscale organization mode (Table 2) are used to investigate instability. Hydrostatic instability (either positive MUCAPE or potential instability) is present for 100% of the mostly convective 3-h periods, 90% of embedded convective within stratiform periods and 58% of the mostly stratiform periods (Table 4). A sounding was considered to have potentially unstable layers if there were at least two 500-m layers with  $d\theta_e/dz < 0$  somewhere in the vertical column. Lifting a potentially unstable layer releases latent potential instability if the air is brought to saturation. Layer lifting occurs in Pacific Northwest cool-season storms via frontal forcing and/or airflow over terrain.

Instability characteristics of embedded convection within stratiform and mostly stratiform have different distributions. Periods with embedded convective within stratiform precipitation had a relative frequency of  $\text{MUCAPE} > 0 \text{ J kg}^{-1}$  approximately 2.8 times that of mostly stratiform precipitation by itself (Table 4). Most of the embedded periods with  $\text{MUCAPE} = 0 \text{ J kg}^{-1}$  were potentially unstable. KSLE soundings without positive MUCAPE but with potentially unstable layers occur in 42% of mostly stratiform soundings as compared to 10% of embedded convection within stratiform soundings.

Figure 9 shows the relationship between different values of MUCAPE and the joint probability distributions of convective precipitation and convective-stratiform intermittency. The set of four figures shows the distribution modes shifting with increasing MUCAPE from left to right along an arch. When no MUCAPE is present, most of the 3-h periods are within the region of the graph labeled as mostly stratiform (Figs. 3 and 9a). As MUCAPE increases, the mode for 3-h periods shifts toward the top of the “arch” corresponding to the embedded convective within stratiform category for MUCAPE between 0 and  $50 \text{ J kg}^{-1}$  (Fig. 9b). The mode moves slightly more toward the mostly convective region of the graph (right side of the figure) for MUCAPE values between 50 and  $150 \text{ J kg}^{-1}$  (Fig. 9c). The small sample

TABLE 4. Assessment of hydrostatic instability for sounding periods with a dominant mode based on whether a sounding has MUCAPE  $> 0$  and/or contains at least two 500-m layers that are potentially unstable ( $d\theta_e/dz < 0$ ). Hydrostatic instability is considered to be present (second column) for a sounding if either MUCAPE is positive or potentially unstable layers are present. (right column) The number of KSLE soundings in each subcategory.

Mode	Percent with hydrostatic instability	Stability criteria	No. of soundings
Mostly stratiform	58%	No MUCAPE, potentially stable	41
		No MUCAPE, potentially unstable	41
		Positive MUCAPE	17
Embedded convective within stratiform	90%	No MUCAPE, potentially stable	4
		No MUCAPE, potentially unstable	17
		Positive MUCAPE	19
Mostly convective	100%	No MUCAPE, potentially stable	0
		No MUCAPE, potentially unstable	3
		Positive MUCAPE	24

size of 23 soundings with MUCAPE  $> 150 \text{ J kg}^{-1}$  (Fig. 9d) makes this last distribution potentially less representative. Figure 9d includes two modes within the mostly convective and mostly stratiform regions of the plot. The MUCAPE values were not high compared to deep moist convection standards. However, these magnitudes of instability appeared to be sufficient for generating cells (section 3c).

The cumulative distribution of the most unstable parcel height indicates that hydrostatic instability during embedded periods was elevated compared to mostly convective periods (Fig. 10). The 50th percentile of the distributions of height of origin for most unstable parcels was 2.5 km for embedded periods versus 0.5 km in mostly convective periods. The distributions of the most unstable parcel height of origin for convective and embedded precipitation were statistically different.

The altitudes where potential instability and shear instability occurred for mostly stratiform, embedded convective within stratiform, and mostly convective periods are compared in Fig. 11. Figure 11a illustrates the frequency of potential instability ( $d\theta_e/dz < 0$ ) at KSLE. Embedded periods had two maxima in frequency of occurrence (near the surface and at 4.5-km altitude). Mostly convective periods had a peak in frequency of potential instability at approximately 2-km altitude. The presence of frontal forcing within the extratropical cyclones likely played a role in realizing potential instability in many embedded periods. Figure 11b illustrates the frequency of vertical wind shear instability (in terms of Ri). The profiles of frequency of vertical wind shear instability were similar among the three modes. Hence, the occurrence of wind shear instability is not a good discriminator in terms of explaining differences in the distributions of generating cells aloft. Vertical wind shear instability preferentially occurred ( $\sim$ one-third of the time) near the surface for all three modes. Very few soundings had much vertical wind shear instability above 2 km.

## 5. Discussion

Differences in sample characteristics and sample sizes are the reasons for the discrepancy between the attribution of generating cells to wind shear instability in the conceptual models of Houze and Medina (2005) and Medina et al. (2007) and our finding that potential instability is the primary source of instability at levels where generating cells occur. Medina et al. (2007) also used data from the KSLE sounding in their analysis. The IMPROVE-2 storms sampled between 26 November and 22 December 2001 and studied in Medina et al. (2007) include only a few examples with freezing heights higher than 1.5-km altitude (Yuter et al. 2011). Houze and Medina (2005) discounted elevated potential instability as a source for generating cells since they found that the air was stable at the levels where updrafts were observed in their two cases (13–14 December 2001 and 28–29 November 2001). In the context of a large sample size of periods with freezing level  $> 1.4$ -km altitude examined in this study, the Medina et al. (2007) conceptual model is true for some cases but does not represent typical conditions.

## 6. Conclusions

The instability characteristics associated with different mesoscale organization modes are examined using six cool seasons (2002–08) of operational scanning radar data near Portland, Oregon (KRTX), and operational sounding data from Salem, Oregon (KSLE). Additionally, five years of MRR vertically pointing radar data from Portland (2005–08) and Merwin, Washington (2010–12), are used to characterize the nature and occurrence of generating cells and fall streaks.

A new method was used to objectively characterize the joint spatial and temporal variability of precipitation over 3-h periods using the time-ordered sequence of

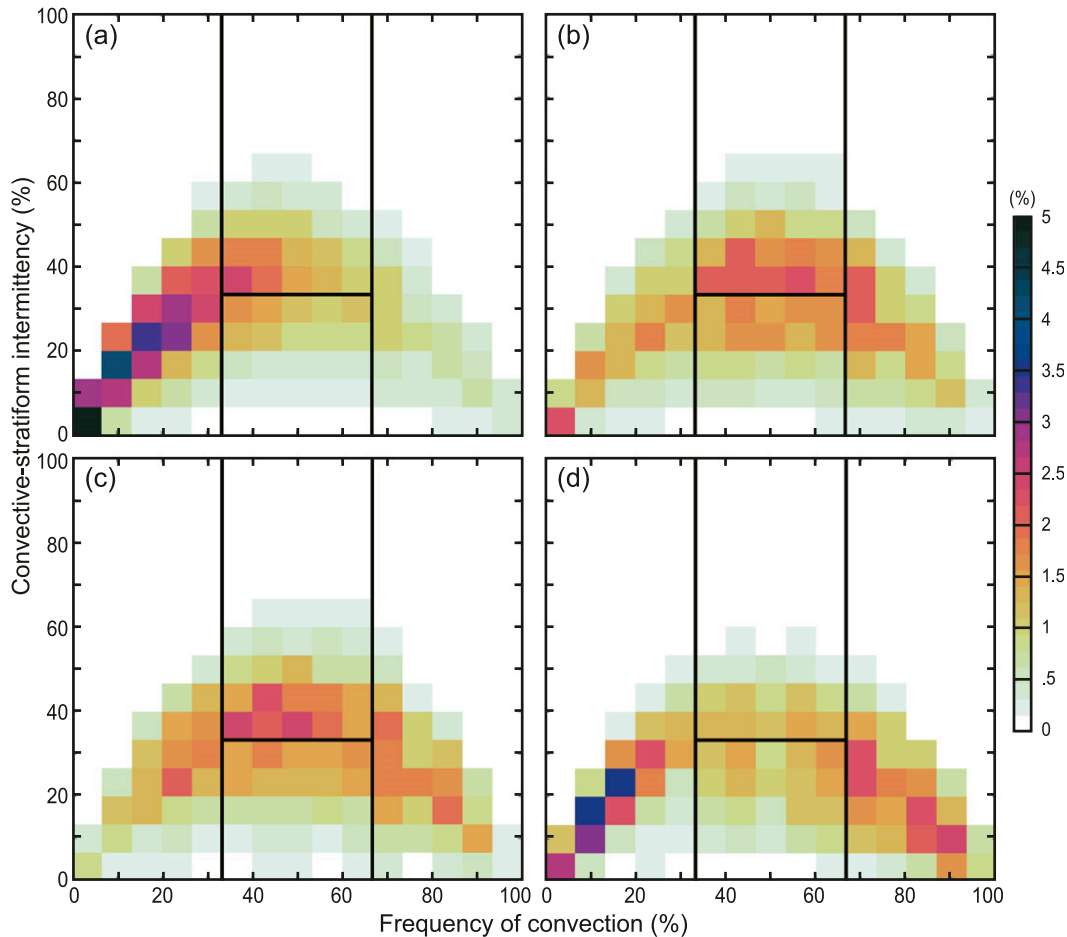


FIG. 9. Joint probability distribution of convective frequency and convective-stratiform intermittency for  $4\text{-km}^2$  gridpoint data for the high freezing level 3-h periods with (a) no MUCAPE (176 soundings), (b)  $0 < \text{MUCAPE} < 50 \text{ J kg}^{-1}$  (99 soundings), (c)  $50 < \text{MUCAPE} < 150 \text{ J kg}^{-1}$  (40 soundings), and (d)  $\text{MUCAPE} > 150 \text{ J kg}^{-1}$  (23 soundings). The frequency of occurrence for each bin is indicated by the shading.

precipitation type at each precipitating grid point. The combination of a new metric, convective-stratiform intermittency, with the classification of radar reflectivity maps into convective and stratiform precipitation types allows us to distinguish periods with embedded convective within stratiform mesoscale organization from those that were mostly convective or mostly stratiform. Embedded convection within stratiform represents conditions when frequent switches between convective and stratiform precipitation structures occur at many individual  $4\text{-km}^2$  grid points within the radar domain. A limitation of the method is that it can only be applied when the lowest elevation angle of the radar scan is within the rain layer. During the six cool seasons, classified storm periods with freezing levels  $>1.4\text{-km}$  altitude composed just under half of the 3-h periods with precipitation area  $>1000 \text{ km}^2$ . The subset of periods classified includes the warmer cool-season storms with

deep rain layers that are climatologically more likely to produce flooding than colder storms (Ralph et al. 2003; Lundquist et al. 2008; Neiman et al. 2008).

Joint frequency distributions of convective frequency and convective-stratiform intermittency illustrate that mesoscale organization occurs in a continuum of states rather than in discrete clusters. Categorical labels are a practical necessity for describing results but the specific boundaries among the categories are somewhat arbitrary. Of the 3-h periods with dominant modes in organization, mostly stratiform precipitation occurs most frequently, and embedded convective within stratiform precipitation occurs more frequently than more isolated convective cells (Table 2). Periods without a dominant mesoscale organization are those with smaller precipitation areas and/or intermediate states.

Early work in the PNW highlighted the roles of generating cells and potential instability aloft (e.g., Hobbs

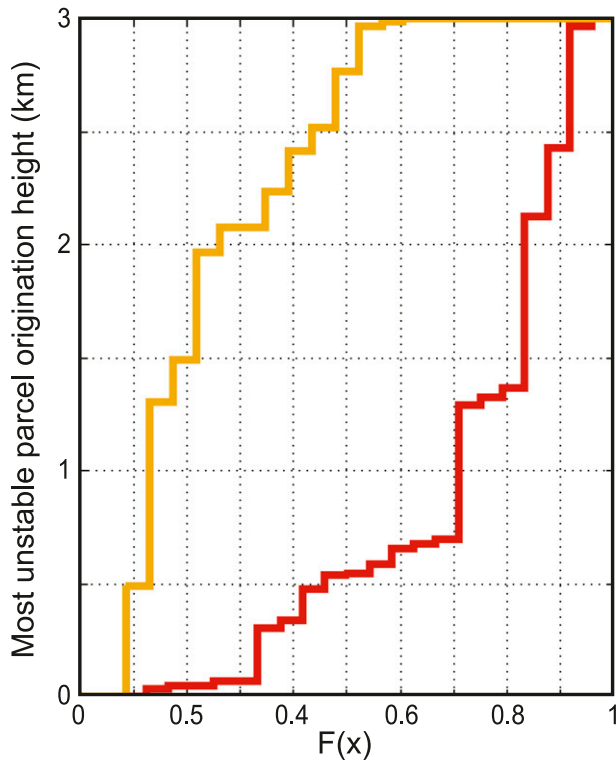


FIG. 10. Cumulative distribution of most unstable parcel origination height from KSLE for periods with mostly convective (red line, 27 soundings) and embedded convective within stratiform (gold line, 40 soundings) mesoscale organization modes.

1978; Hobbs and Locatelli 1978; Parsons and Hobbs 1983). Our results are consistent with this previous work and recent work by Evans et al. (2005) and Woods et al. (2005). Generating cells aloft are common in Portland

region storms and are primarily associated with potential instability aloft.

The MRR reflectivity data showed nearly ubiquitous fall streaks in snow originating above 3 km for mostly stratiform and embedded 3-h periods. Stronger generating cells enhance reflectivity in the rain layer consistent with a seeder mechanism. Stronger generating cells occurred more commonly during embedded periods than mostly stratiform periods as evidenced by more variable and higher maximum values of MRR Doppler vertical velocities within the snow layer during embedded periods.

Hydrostatic instability more typically occurred at higher altitudes for embedded convective within stratiform periods compared to mostly convective periods (Fig. 11). The origination heights for most unstable parcels were more commonly elevated ( $>2.5$  km) for embedded periods compared to mostly convective periods (Fig. 10). There was a double maximum in potential instability near the surface and at 4.5-km altitude during embedded periods compared to the peak potential instability at 2-km altitude during mostly convective periods. Almost 90% of embedded periods have active or latent (potential) instability as compared to 58% for mostly stratiform periods (Table 4). The embedded periods had a nearly 3 times higher relative proportion of times with  $\text{MUCAPE} > 0 \text{ J kg}^{-1}$  compared to mostly stratiform periods. Most of the embedded periods with  $\text{MUCAPE} = 0 \text{ J kg}^{-1}$  were also potentially unstable. Vertical wind shear instability is present but primarily occurred below 2-km altitude (Fig. 11). The attribution of generating cells to wind shear instability in the conceptual model of Houze and Medina (2005) and

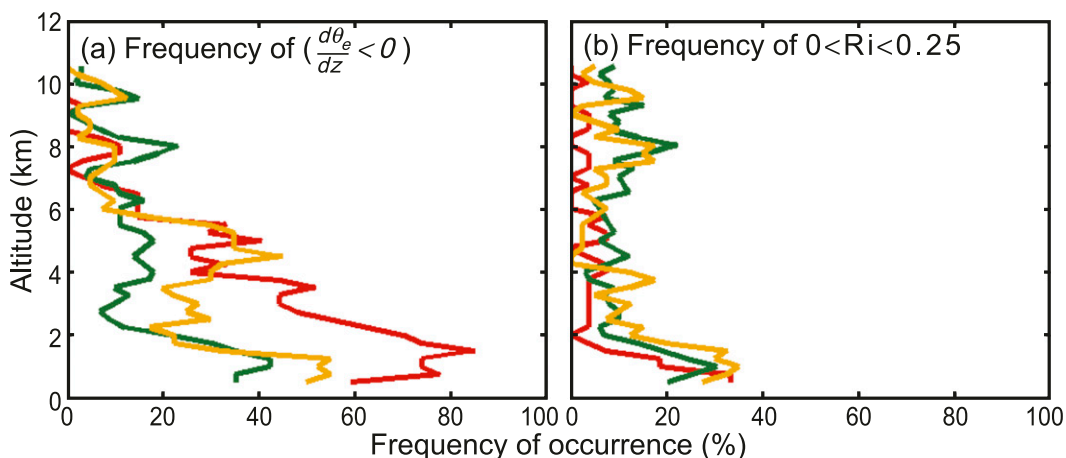


FIG. 11. Vertical profiles of the frequency of potential instability and shear instability for KSLE soundings corresponding to times with a dominant mesoscale organization mode. (a) Frequency of potential instability [ $d\theta_e/dz < 0$ ] and (b) frequency of vertical wind shear instability ( $0 < \text{Ri} < 0.25$ ). Red lines are mostly convective 3-h periods, gold lines are embedded convective within stratiform 3-h periods, and green lines are mostly stratiform 3-h periods. Values are calculated over 500-m layers.

Medina et al. (2007) is not consistent with typical conditions in the dataset examined in this study.

Additional observations are needed to address the sources of the elevated hydrostatic instability, including the roles of synoptic features (e.g., frontal circulations and conditional symmetric instability) and terrain features on developing environmental conditions conducive to elevated generating cells. Information on the life cycle of convective cells embedded within stratiform precipitation as compared to those in convective regions would also be of value in understanding the underlying physics of precipitation variability. Information on how generating cells respond to the terrain of the Coastal Range and the Cascade Mountains will help connect the work of this study with other work on orographic precipitation enhancement in this region.

Current operational and idealized numerical models use horizontal grid spacing of 3 km, 1.3 km, and smaller. Generating cells aloft within cool-season extratropical cyclones are relevant for precipitation variability and accumulation at these smaller scales. Ensuring that numerical weather prediction models adequately capture hydrostatic instability aloft, generating cells and fall streaks will likely improve the precipitation fields especially within the warm sector of extratropical cyclones where most of the precipitation accumulation occurs (Neiman et al. 2008; Ralph et al. 2011).

*Acknowledgments.* Special thanks to Matthew Parker, Karl Wegmann, Sankar Arumugam, David Kingsmill, Brian Colle, Matthew A. Miller, Casey Burleyson, Nathan Hardin, Matthew Woelfle, John L'Heureux, and Andrew Hall for advice and technical support. Beth Tully provided graphics support. We also thank two anonymous reviewers for their constructive comments that helped improve the paper. Perusal time–height images of MRR data collected in Portland, Oregon, from 2005 to 2012 and Merwin, Washington, from 2010 to 2012 are accessible online ([ftp://precip.meas.ncsu.edu/pub/mrr+/tools/MRR\\_top\\_level.html](ftp://precip.meas.ncsu.edu/pub/mrr+/tools/MRR_top_level.html)).

The generous support of the U.S. Air Force and the Air Force Institute of Technology's Civilian Institution Programs made this research possible; however, the views expressed in this document are those of the authors and do not reflect the official policy or position of the U.S. Air Force, Department of Defense, or the U.S. government. This material is also based upon work supported by the National Science Foundation under Grant ATM-0908420 (Yuter). Any opinions, findings, and conclusions or recommendations expressed in this material are those of the author(s) and do not necessarily reflect the views of the National Science Foundation.

## REFERENCES

- Bader, M. J., G. S. Forbes, J. R. Grant, R. B. E. Lilley, and A. J. Waters, 1995: *Images in Weather Forecasting: A Practical Guide for Interpreting Satellite and Radar Imagery*. University Press, 499 pp.
- Bao, J.-W., S. A. Michelson, P. J. Neiman, F. M. Ralph, and J. M. Wilczak, 2006: Interpretation of enhanced integrated water vapor bands associated with extratropical cyclones: Their formation and connection to tropical moisture. *Mon. Wea. Rev.*, **134**, 1063–1080, doi:10.1175/MWR3123.1.
- Baum, R. L., and J. W. Godt, 2010: Early warning of rainfall-induced shallow landslides and debris flows in the USA. *Landslides*, **7**, 259–272, doi:10.1007/s10346-009-0177-0.
- Biasutti, M., S. E. Yuter, C. D. Burleyson, and A. H. Sobel, 2012: Very high resolution rainfall patterns measured by TRMM precipitation radar: Seasonal and diurnal cycles. *Climate Dyn.*, **39**, 239–258, doi:10.1007/s00382-011-1146-6.
- Browning, K. A., 1974: Mesoscale structure of rain systems in the British Isles. *J. Meteor. Soc. Japan*, **52**, 314–327.
- , 1986: Conceptual models of precipitation systems. *Wea. Forecasting*, **1**, 23–41, doi:10.1175/1520-0434(1986)001<0023:CMOPS>2.0.CO;2.
- , and F. F. Hill, 1981: Orographic rain. *Weather*, **36**, 326–328, doi:10.1002/j.1477-8696.1981.tb05354.x.
- , and G. A. Monk, 1982: A simple model for the synoptic analysis of cold fronts. *Quart. J. Roy. Meteor. Soc.*, **108**, 435–452, doi:10.1002/qj.49710845609.
- , F. F. Hill, and C. W. Pardoe, 1974: Structure and mechanism of precipitation and the effect of orography on wintertime warm sector. *Quart. J. Roy. Meteor. Soc.*, **100**, 309–330, doi:10.1002/qj.49710042505.
- Cannon, D. J., D. J. Kirshbaum, and S. L. Gray, 2012: Under what conditions does embedded convection enhance orographic precipitation? *Quart. J. Roy. Meteor. Soc.*, **138**, 391–406, doi:10.1002/qj.926.
- Churchill, D. D., and R. A. Houze, 1984: Development and structure of winter monsoon cloud clusters on 10 December 1978. *J. Atmos. Sci.*, **41**, 933–960, doi:10.1175/1520-0469(1984)041<0933:DASOWM>2.0.CO;2.
- Doswell, C. A., and E. N. Rasmussen, 1994: The effect of neglecting the virtual temperature correction on CAPE calculations. *Wea. Forecasting*, **9**, 625–629, doi:10.1175/1520-0434(1994)009<0625:TEONTV>2.0.CO;2.
- Doviak, R. J., and D. S. Zrnic, 1993: *Doppler Radar and Weather Observations*. 2nd ed. Dover Publications, 562 pp.
- Elliott, R. D., and E. L. Hovind, 1964: On convection bands within Pacific Coast storms and their relation to storm structure. *J. Appl. Meteor.*, **3**, 143–154, doi:10.1175/1520-0450(1964)003<0143:OCBWPC>2.0.CO;2.
- Ellis, T. D., T. L'Ecuyer, J. M. Haynes, and G. L. Stephens, 2009: How often does it rain over the global oceans? The perspective from CloudSat. *Geophys. Res. Lett.*, **36**, L03815, doi:10.1029/2008GL036728.
- Evans, A. G., J. D. Locatelli, M. T. Stoelinga, and P. V. Hobbs, 2005: The IMPROVE-1 storm of 1–2 February 2001. Part II: Cloud structures and the growth of precipitation. *J. Atmos. Sci.*, **62**, 3456–3473, doi:10.1175/JAS3547.1.
- Fuhrer, O., and C. Schar, 2005: Embedded cellular convection in moist flow past topography. *J. Atmos. Sci.*, **62**, 2810–2828, doi:10.1175/JAS3512.1.
- Glickman, T., Ed., 2000: *Glossary of Meteorology*. 2nd ed. Amer. Meteor. Soc., 855 pp.

- Hobbs, P. V., 1978: Organization and structure of clouds and precipitation on the mesoscale and microscale in cyclonic storms. *Rev. Geophys. Space Phys.*, **16**, 741–755, doi:10.1029/RG016i004p00741.
- , and J. D. Locatelli, 1978: Rainbands, precipitation cores and generating cells in a cyclonic storm. *J. Atmos. Sci.*, **35**, 230–241.
- , T. J. Matejka, P. H. Herzegh, J. D. Locatelli, and R. A. Houze, 1980: The mesoscale and microscale structure and organization of clouds and precipitation in midlatitude cyclones. I: A case study of a cold front. *J. Atmos. Sci.*, **37**, 568–596, doi:10.1175/1520-0469(1980)037<0568:TMAMSA>2.0.CO;2.
- Houze, R. A., 1997: Stratiform precipitation in regions of convection: A meteorological paradox? *Bull. Amer. Meteor. Soc.*, **78**, 2179–2196, doi:10.1175/1520-0477(1997)078<2179:SPIROC>2.0.CO;2.
- , and S. Medina, 2005: Turbulence as a mechanism for orographic precipitation enhancement. *J. Atmos. Sci.*, **62**, 3599–3623, doi:10.1175/JAS3555.1.
- James, C. N., and R. A. Houze, 2005: Modification of precipitation by coastal orography in storms crossing northern California. *Mon. Wea. Rev.*, **133**, 3110–3131, doi:10.1175/MWR3019.1.
- Kessler, E., 1969: *On the Distribution and Continuity of Water Substance in Atmospheric Circulation*. Meteor. Monogr., No. 10, Amer. Meteor. Soc., 84 pp.
- Kirshbaum, D. J., and R. B. Smith, 2008: Temperature and moist-stability effects on midlatitude orographic precipitation. *Quart. J. Roy. Meteor. Soc.*, **134**, 1183–1199, doi:10.1002/qj.274.
- Kreitzberg, C. W., and H. A. Brown, 1970: Mesoscale weather systems within an occlusion. *J. Appl. Meteor.*, **9**, 417–432, doi:10.1175/1520-0450(1970)009<0417:MWSWAO>2.0.CO;2.
- Lin, Y., B. A. Colle, and S. E. Yuter, 2013: Impact of moisture flux and freezing level on simulated orographic precipitation errors over the Pacific Northwest. *J. Hydrometeorol.*, **14**, 140–152, doi:10.1175/JHM-D-12-019.1.
- Löffler-Mang, M., M. Kunz, and W. Schmidt, 1999: On the performance of a low-cost K-band Doppler radar for quantitative rain measurement. *J. Atmos. Oceanic Technol.*, **16**, 379–387, doi:10.1175/1520-0426(1999)016<0379:OTPOAL>2.0.CO;2.
- Lundquist, J. D., P. J. Neiman, B. Martner, A. B. White, D. J. Gattas, and F. M. Ralph, 2008: Rain versus snow in the Sierra Nevada, California: Comparing Doppler profiling radar and surface observations of melting level. *J. Hydrometeorol.*, **9**, 194–211, doi:10.1175/2007JHM853.1.
- Markowski, P., and Y. Richardson, 2010: *Mesoscale Meteorology in Midlatitudes*. Wiley-Blackwell, 407 pp.
- Marshall, J. S., 1953: Precipitation trajectories and patterns. *J. Meteor.*, **10**, 25–29, doi:10.1175/1520-0469(1953)010<0025:PTAP>2.0.CO;2.
- Matejka, T. J., R. A. Houze Jr., and P. V. Hobbs, 1980: Microphysics and dynamics of clouds associated with extratropical cyclones. *Quart. J. Roy. Meteor. Soc.*, **106**, 29–56, doi:10.1002/qj.49710644704.
- McCann, D. W., 1995: Three-dimensional computations of equivalent potential vorticity. *Wea. Forecasting*, **10**, 798–802, doi:10.1175/1520-0434(1995)010<0798:TDCOEP>2.0.CO;2.
- Medina, S., E. Sukovich, and R. A. Houze, 2007: Vertical structures of precipitation in cyclones crossing the Oregon Cascades. *Mon. Wea. Rev.*, **135**, 3565–3586, doi:10.1175/MWR3470.1.
- Nagle, R. E., and S. M. Serebreny, 1962: Radar precipitation echo and satellite cloud observations of a maritime cyclone. *J. Appl. Meteor.*, **1**, 279–295, doi:10.1175/1520-0450(1962)001<0279:RPEASC>2.0.CO;2.
- NCAR, cited 2012: REORDER software. [Available online at <https://wiki.ucar.edu/display/raygridding/Reorder+Gridding+Software>.]
- NCDC, cited 2012: Storm events database. [Available online at <http://www.ncdc.noaa.gov>.]
- Neiman, P. J., F. M. Ralph, G. A. Wick, J. D. Lundquist, and M. D. Dettinger, 2008: Meteorological characteristics and overland precipitation impacts of atmospheric rivers affecting the west coast of North America based on eight years of SSM/I satellite observations. *J. Hydrometeorol.*, **9**, 22–47, doi:10.1175/2007JHM855.1.
- OFCM, 2006: WSR-88D unit description and operational applications. Doppler Radar Meteorological Observations. Federal Meteorological Handbook 11, Part D, FCM-H11D-2006, 218 pp. [Available online at <http://www.ofcm.gov/fmh11/fmh11partd/pdf/FMH11D-2006.pdf>.]
- Panziera, L., and U. Germann, 2010: The relationship between airflow and orographic precipitation in the Southern Alps as revealed by weather radar. *Quart. J. Roy. Meteor. Soc.*, **136**, 222–238, doi:10.1002/qj.544.
- Parsons, D. B., and P. V. Hobbs, 1983: The mesoscale and microscale structure and organization of clouds and precipitation in midlatitude cyclones. XI: Comparisons between observational and theoretical aspects of rainbands. *J. Atmos. Sci.*, **40**, 2377–2397, doi:10.1175/1520-0469(1983)040<2377:TMAMSA>2.0.CO;2.
- Peters, G., B. Fischer, and T. Andersson, 2002: Rain observations with a vertically looking Micro Rain Radar (MRR). *Boreal Environ. Res.*, **7**, 353–362.
- Ralph, F. M., P. J. Neiman, D. E. Kingsmill, P. O. G. Persson, A. B. White, E. T. Strem, E. D. Andrews, and R. C. Antweiler, 2003: The impact of a prominent rain show on flooding in California's Santa Cruz Mountains: A CALJET case study and sensitivity to ENSO cycle. *J. Hydrometeorol.*, **4**, 1243–1264, doi:10.1175/1525-7541(2003)004<1243:TIOAPR>2.0.CO;2.
- , —, and R. Rotunno, 2005: Dropsonde observations in low-level jets over the northeastern Pacific Ocean from CALJET-1998 and PACJET-2001: Mean vertical-profile and atmospheric-river characteristics. *Mon. Wea. Rev.*, **133**, 889–910, doi:10.1175/MWR2896.1.
- , P. J. Neiman, G. N. Kiladis, K. Weickmann, and D. W. Reynolds, 2011: A multiscale observational case study of a Pacific atmospheric river exhibiting tropical–extratropical connections and a mesoscale frontal wave. *Mon. Wea. Rev.*, **139**, 1169–1189, doi:10.1175/2010MWR3596.1.
- Rauber, R. M., and Coauthors, 2014: Stability and charging characteristics of the comma head region of continental winter cyclones. *J. Atmos. Sci.*, in press.
- Rinehart, R. E., 2004: *Radar for Meteorologists*. 4th ed. Rinehart Publications, 482 pp.
- Rosenow, A. A., D. M. Plummer, R. M. Rauber, G. M. McFarquhar, B. F. Jewett, and D. Leon, 2014: Vertical velocity and physical structure of generating cells and convection in the comma head region of continental winter cyclones. *J. Atmos. Sci.*, in press.
- Rutledge, S. A., and P. V. Hobbs, 1983: The mesoscale and microscale structure and organization of clouds and precipitation in midlatitude cyclones. VIII: A model for the “seeder-feeder” process in warm-frontal rainbands. *J. Atmos. Sci.*, **40**, 1185–1206, doi:10.1175/1520-0469(1983)040<1185:TMAMSA>2.0.CO;2.
- Schultz, D. M., and P. N. Schumacher, 1999: The use and misuse of conditional symmetric instability. *Mon. Wea. Rev.*, **127**, 2709–2732, doi:10.1175/1520-0493(1999)127<2709:TUAMOC>2.0.CO;2.
- , and W. J. Steenburgh, 1999: The formation of a forward-tilting cold front with multiple cloud bands during Superstorm 1993. *Mon.*

- Wea. Rev.*, **127**, 1108–1124, doi:[10.1175/1520-0493\(1999\)127<1108:TFOAFT>2.0.CO;2](https://doi.org/10.1175/1520-0493(1999)127<1108:TFOAFT>2.0.CO;2).
- Steiner, M., R. A. Houze, and S. E. Yuter, 1995: Climatological characterization of three-dimensional storm structure from operational radar and rain gauge data. *J. Appl. Meteor.*, **34**, 1978–2007, doi:[10.1175/1520-0450\(1995\)034<1978:CCOTDS>2.0.CO;2](https://doi.org/10.1175/1520-0450(1995)034<1978:CCOTDS>2.0.CO;2).
- Stoelinga, M. T., and Coauthors, 2003: Improvement of Microphysical Parameterization through Observational Verification Experiment. *Bull. Amer. Meteor. Soc.*, **84**, 1807–1826, doi:[10.1175/BAMS-84-12-1807](https://doi.org/10.1175/BAMS-84-12-1807).
- , R. E. Stewart, G. Thompson, and J. M. Thériault, 2013: Microphysical processes within winter orographic cloud and precipitation systems. *Mountain Weather Research and Forecasting*, F. K. Chow, S. F. J. de Wekker, and B. J. Snyder, Eds., Springer, 345–408, doi:[10.1007/978-94-007-4098-3\\_7](https://doi.org/10.1007/978-94-007-4098-3_7).
- Westrick, K. J., and C. F. Mass, 2001: An evaluation of a high-resolution hydrometeorological modeling system for prediction of a cool-season flood event in a coastal mountainous watershed. *J. Hydrometeor.*, **2**, 161–179, doi:[10.1175/1525-7541\(2001\)002<0161:AEOAHR>2.0.CO;2](https://doi.org/10.1175/1525-7541(2001)002<0161:AEOAHR>2.0.CO;2).
- Wilks, D. S., 2006: *Statistical Methods in the Atmospheric Sciences*. 2nd ed. Elsevier, 627 pp.
- Woods, P. W., M. T. Stoelinga, J. D. Locatelli, and P. V. Hobbs, 2005: Microphysical processes and synergistic interaction between frontal and orographic forcing of precipitation during the 13 December 2001 IMPROVE-2 event over the Oregon Cascades. *J. Atmos. Sci.*, **62**, 3493–3519, doi:[10.1175/JAS3550.1](https://doi.org/10.1175/JAS3550.1).
- Yuter, S. E., and R. A. Houze, 1997: Measurements of raindrop size distributions over the Pacific warm pool and implications for Z–R relations. *J. Appl. Meteor.*, **36**, 847–867, doi:[10.1175/1520-0450\(1997\)036<0847:MORSDO>2.0.CO;2](https://doi.org/10.1175/1520-0450(1997)036<0847:MORSDO>2.0.CO;2).
- , —, E. A. Smith, T. T. Wilheit, and E. Zipser, 2005: Physical characterization of tropical oceanic convection observed in KWAJEX. *J. Appl. Meteor.*, **44**, 385–414, doi:[10.1175/JAM2206.1](https://doi.org/10.1175/JAM2206.1).
- , D. A. Stark, J. A. Crouch, M. J. Payne, and B. A. Colle, 2011: The impact of varying environmental conditions on the spatial and temporal patterns of orographic precipitation over the Pacific Northwest near Portland, Oregon. *J. Hydrometeor.*, **12**, 329–351, doi:[10.1175/2010JHM1239.1](https://doi.org/10.1175/2010JHM1239.1).
- Zhu, Y., and R. E. Newell, 1998: A proposed algorithm for moisture fluxes from atmospheric rivers. *Mon. Wea. Rev.*, **126**, 725–733, doi:[10.1175/1520-0493\(1998\)126<0725:APAFMF>2.0.CO;2](https://doi.org/10.1175/1520-0493(1998)126<0725:APAFMF>2.0.CO;2).